Materials Advances

ROYAL SOCIETY OF CHEMISTRY

PAPER

View Article Online
View Journal | View Issue

Cite this: *Mater. Adv.*, 2026, 7, 2465

$CsPbBr_3$ nanocrystals supported on a partially oxidized Ti_2N MXene for photothermal CO_2 conversion

Kevin Mego, [a] Emanuela Accardo, [b] Pedro Ruiz-Campos, [c] Herme G. Baldoví *[b] and Pedro Atienzar *[a]

Received 30th September 2025,
Accepted 22nd December 2025

DOI: 10.1039/d5ma01122a

rsc.li/materials-advances

The development of new photo-thermal catalysts for the transformation of CO_2 into fuels is of great interest, offering a clean and sustainable approach to reducing the carbon footprint. Herein, we present a novel hybrid material composed of a nanocrystalline metal halide perovskite ($CsPbBr_3$) supported on a two-dimensional titanium nitride (Ti_2N) MXene. Additionally, we demonstrate the importance of forming an external TiO_2 layer through partial oxidation of the MXene (POM–Ti_2N), which introduces catalytic centers and enhances photogenerated charge separation. Remarkable activity in the formation of CH_4 and CO was observed, with yields of 321 μmol g^{-1} and 480 μmol g^{-1}, respectively. The selectivity of the reaction was found to be temperature dependent. The mechanism was thoroughly investigated using XPS and photoluminescence studies. XPS analysis revealed a significant chemical interaction between the $CsPbBr_3$ nanocrystals and the POM–Ti_2N MXene after the formation of the composite. Photoluminescence measurements revealed a considerably shorter emission lifetime for the hybrid catalyst (τ_{ave} = 1.73 ns) compared to that of the $CsPbBr_3$ nanoparticles (τ_{ave} = 25.32 ns), indicating strong interaction with the MXene. Furthermore, this research highlights the potential of combining metal halide perovskites with MXenes and the importance of controlling their interface for photo-thermal reactions.

1. Introduction

Researchers are making significant efforts to address climate change by developing CO_2 utilization technologies that convert this molecule into chemicals. Solar-driven photothermal catalysis is a compelling and sustainable approach that harnesses light and heat energy to synergistically convert CO_2 into fuels and valuable chemicals.[1,2] There are many photothermal catalytic pathways that offer sustainable routes for CO_2 valorization,[3,4] such as the Sabatier reaction, which has been one of the most studied reactions for over a century since its discovery. This reaction consists of the hydrogenation of CO_2 to CH_4, which is thermodynamically favorable but is hindered by slow reaction kinetics; therefore, the use of high temperatures is necessary to activate the CO_2 molecule. The photothermal catalytic mechanism includes multiple proton-coupled electron transfer to CO_2 to form CH_4, which requires control of intermediate species on catalytic surfaces, often resulting in reduced selectivity and lower overall activity.[5]

In the classical thermal methanation process, the most studied metallic active centers are Ni, Ru, and Rh, which require high temperatures (300 to 400 °C) and pressures (5–20 bar) to achieve high efficiencies. However, the photothermal pathway can promote the Sabatier reaction under milder conditions, employing the same active sites supported on a semiconductor, with metal oxides being the most commonly used due to their robustness under reaction conditions. Recent studies showed that nickel (Ni) has emerged as an optimal compromise, delivering Ru-like activity when properly nanostructured on TiO_2 or CeO_2 supports.[6–8] Other researchers used single atoms and nanoparticles of ruthenium supported on $CeAlO_x$, achieving formidable catalytic performances.[9] Although a huge number of materials have been already explored to boost the photocatalytic side of the photothermal reaction (*e.g.* metal oxides, MOFs, COFs, metal complexes, C_3N_4...),[10–13] there is still a need to boost this reaction at lower temperatures (<250 °C).

Metal halide perovskite nanocrystal (NC) semiconductors have been extensively studied because they offer a wide range of applications due to their excellent optoelectronic properties, such as broad absorption in the UV-vis spectrum, tunable light

[a] *Instituto de Tecnología Química, Consejo Superior de Investigaciones Científicas, Universitat Politècnica de València, Avenida de los Naranjos s/n, 46022, Valencia, Spain. E-mail: pedatcor@itq.upv.es*
[b] *Departamento de Química, Universitat Politècnica de València, Camino de Vera s/n, 46022, Valencia, Spain. E-mail: hergarba@itq.upv.es*
[c] *Universidad Científica del Sur, Panamericana Sur Km 19, 150142, Lima, Peru*

absorption range, long charge diffusion length, and high molar extinction coefficients.[14] All these properties make them potential candidates for multiple photocatalytic applications. However, to improve the photocatalytic activity of pristine $CsPbBr_3$, it has been combined with other materials, on the one hand, to improve charge separation properties through charge migration and, on the other hand, to add better active catalytic sites.[15,16] In this regard, MXene materials as a new class of two-dimensional (2D) structures have recently attracted great attention due to their interesting properties such as rich surface chemistry, modifiable electronic structure and thermal stability. MXenes are transition metal carbides or nitrides with the general formula $M_{n+1}X_nT_x$ (n = 1, 2 or 3), where M corresponds to a transition metal, X can be C or N, and T_x indicates the surface functional groups (usually –F, –O or –OH). These functional groups play an important role in the adsorption/desorption of molecules and electron transfer properties. Currently, in photothermal reduction of CO_2, there are a few examples in the literature studying the catalytic properties of MXene carbides containing perovskite NCs. For instance, aerogels of a $CsPbBr_3/Ti_3C_2T_x$ MXene showed that the $Ti_3C_2T_x$ MXene's conductive network promotes charge separation from photoexcited $CsPbBr_3$, while its surface terminations (–O, –F, –and OH) improve CO_2 adsorption, outperforming individual components.[17]

In addition, partially oxidized 2D transition metal carbide MXenes also offer the possibility to decorate the titanium nitride MXene with TiO_2 moieties. According to the work of Pazniak *et al.*,[18] the enhanced charge carrier exchange at the TiO_2/MXene interface enhances the sensing properties due to the formation of a depletion region between the metal and the semiconductor interface.[19]

The novelty of this work lies in the use of the titanium nitride (Ti_2N) MXene in the Sabatier reaction for the first time. Therefore, within this context, we have been the first investigating the formation of a novel hybrid material composed of nanocrystalline $CsPbBr_3$ supported on a two-dimensional titanium nitride (Ti_2N) MXene for photo-thermal CO_2 conversion. To date, there has been no report describing this specific combination. Although bare metal nitride MXenes can exhibit certain limitations in this reaction, we addressed this by forming external TiO_2 moieties through partial oxidation of the Ti_2N MXene and combining it with the perovskite nanocrystals. We evaluated catalytic activity under different conditions and assessed its reusability, concluding that this hybrid is capable of performing CO_2 revalorization. XPS analysis and photophysical studies were carried out. Finally, we propose a working mechanism based on the formation of a heterojunction architecture, featuring an interlayer that inhibits direct charge recombination.

2. Results and discussion

$CsPbBr_3$ perovskite NCs and the Ti_2N MXene were prepared separately according to the synthetic procedure described in detail in the Materials and Methods section (see SI) and illustrated in Scheme 1. The synthesis of $CsPbBr_3$ NCs was carried out by the hot injection method.[20] Scheme 1a shows the conventional preparation of the NCs through three sequential steps: (i) mixing the precursors in a three-neck flask at elevated temperature, (ii) rapid injection of the cesium precursor, and (iii) immediate quenching in an ice-cold water bath.

The preparation of the partially oxidized multilayer Ti_2N MXene (POM–Ti_2N) involves two main stages: (i) first the MAX phase was treated with $CuCl_2$ using the molten salt method at high temperature (650 °C), followed by copper removal using persulfate solution, and (ii) afterwards the solid was filtered and thoroughly washed with deionized water. It is during the purification with persulfate salts at 70 °C that a thin layer of small nanoparticles of TiO_2 was grown on top of the surface resulting in the partial oxidation of the Ti_2N MXene. (see Scheme 1b). Actually, TiO_2's presence is residual if the purification is carried out during the same time and at room temperature.

Finally, the perovskite NCs were supported on POM–Ti_2N by dispersing POM–Ti_2N by ultrasonication in hexane and adding dropwise a concentrated suspension of NCs. After some time, the solid was recovered by filtration. More details are described in the Materials and methods section in the SI (Scheme 1c).

The synthesis of M–Ti_2N was carried out according to the publication by Xinbo Liu *et al.*, following the molten salt method, in which molar ratios of 1 : 3 and 1 : 4 with respect to $Ti_2NAl : CuCl_2$ were used. In our case, a ratio of 1 : 4 was chosen to synthesise the multi-layered T_2N MXene.[21] In fact, analysis carried out with X-ray diffraction spectroscopy shown in Fig. S4 confirms that the titanium nitride MXene synthesized by the molten salt method leads to a nitride with the crystal structure of α-TiN with characteristic peaks at 37.9°, 43.3° and 62.7° corresponding, respectively, to the planes (004), (103), and (110).[22,23]

A slight modification of the purification procedure during the bath with persulphate salts, such as raising the temperature of the process or increasing the concentration of these salts, leads to modification of the chemistry of the surface of the MXene layers by superficially oxidising the M–Ti_2N layers as can also be seen in Fig. S4 with the appearance of new TiO_2-related signals at 2θ = 25.3°, 47.9°, and 54.4° and 2θ = 27.4° and 43.3° assigned to (101), (202), and (211) anatase and (110) and (111) rutile crystalline planes.

Furthermore, XRD analyses were performed for all the materials. The XRD results were consistent with the ICSD data file #204325,[24] which confirms the cubical crystalline structure of the $CsPbBr_3$ NCs, evidenced by the presence of the peaks at the angles 15° and 30°, which represent the (001) and (002) crystalline planes of the cubic perovskite crystals (Fig. 1b). Once the NCs@POM–Ti_2N composite has been formed, it is not possible to visualise the signals due to the low concentration of NCs in the sample (< 5% by weight) and the small amount of material used during the analysis (Fig. 1a).

Moreover, high-resolution transmission electron microscopy (HR-TEM) was used to study the $CsPbBr_3$ NCs and the

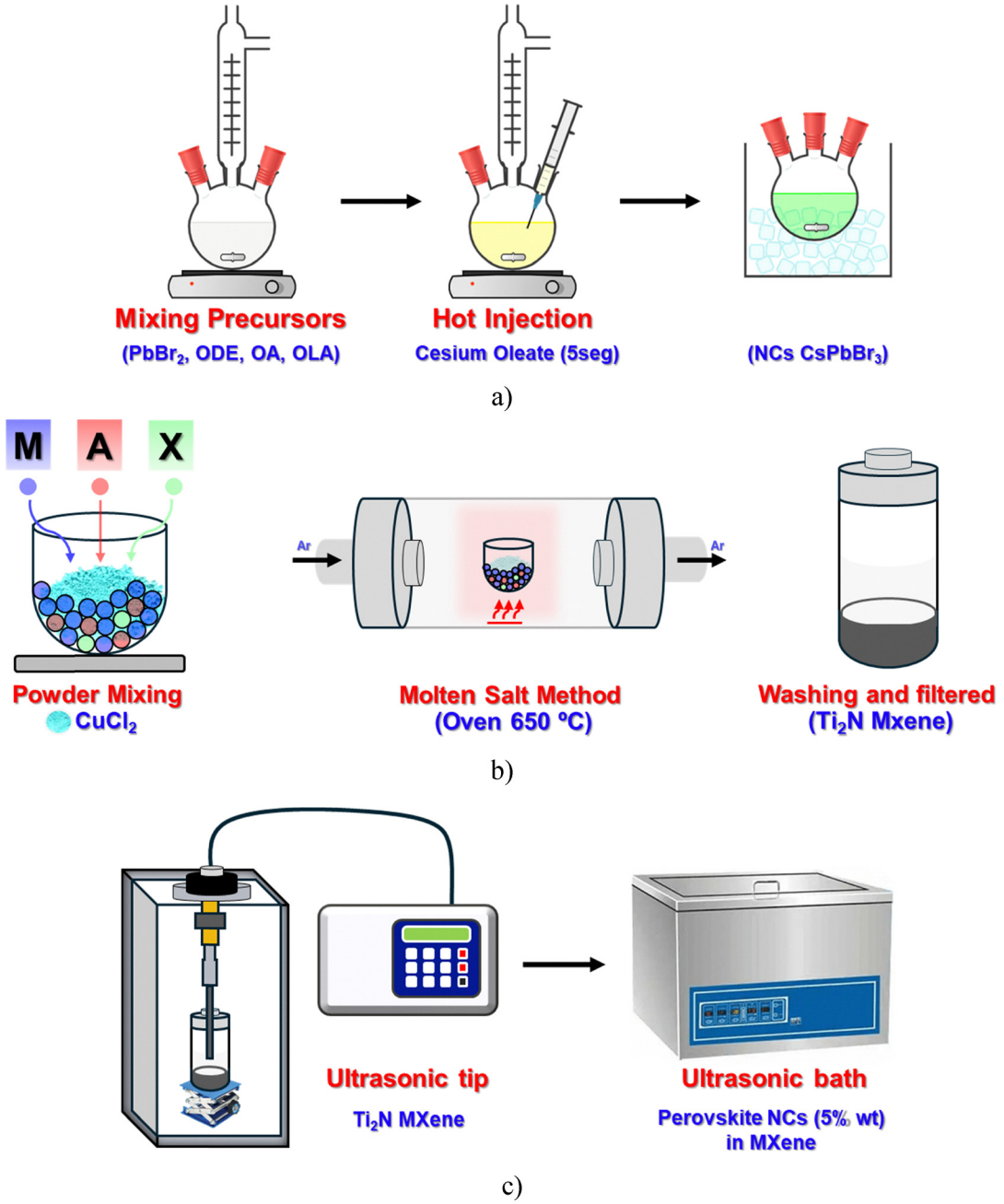

Scheme 1 Synthetic procedure for the preparation of the catalyst. (a) Preparation of the $CsPbBr_3$ NCs, (b) formation of the Ti_2N MXene from the MAX phase and (c) the impregnation process for the deposition of the $CsPbBr_3$ NCs on the exfoliated Ti_2N MXene.

Ti_2N MXene independently. Fig. 2a shows that the perovskite NC particles have a similar size and crystallinity. The particle size distribution of NCs was estimated using HR-TEM, yielding an average size of 5 nm (Fig. 2b).

High resolution field emission scanning electron microscopy (HR-FESEM) is a useful tool to distinguish between the formation of a multi-layered Ti_2N MXene (M–Ti_2N) and POM–Ti_2N. A soft purification treatment with 0.1 M sodium persulfate at room temperature leads easily to purification of M-Ti_2N with a minor structural defect, as shown in Fig. 2c, whereas the same concentration of persulfate, but treating the MXene at 70 °C, resulted in slight oxidation of the MXene surface, forming POM–Ti_2N (see Fig. 2d). Also, HR-FESEM images in Fig. S5 reveal the formation of rugosity on the surface and edges of the Ti_2N MXene layers with the appearance of small crystals of TiO_2 homogenously dispersed. Additionally, interplanar distances measured using HR-TEM on layers of the POM–T_2N sample confirm the simultaneous presence of Ti_2N and TiO_2 crystals (Fig. 2e) After the formation of the composite NCs@POM–Ti_2N no evident changes are seen by HR-FESEM in the partially oxidized MXene particle (Fig. 2f); however, the dispersion of NC particles on the POM–Ti_2N MXene is

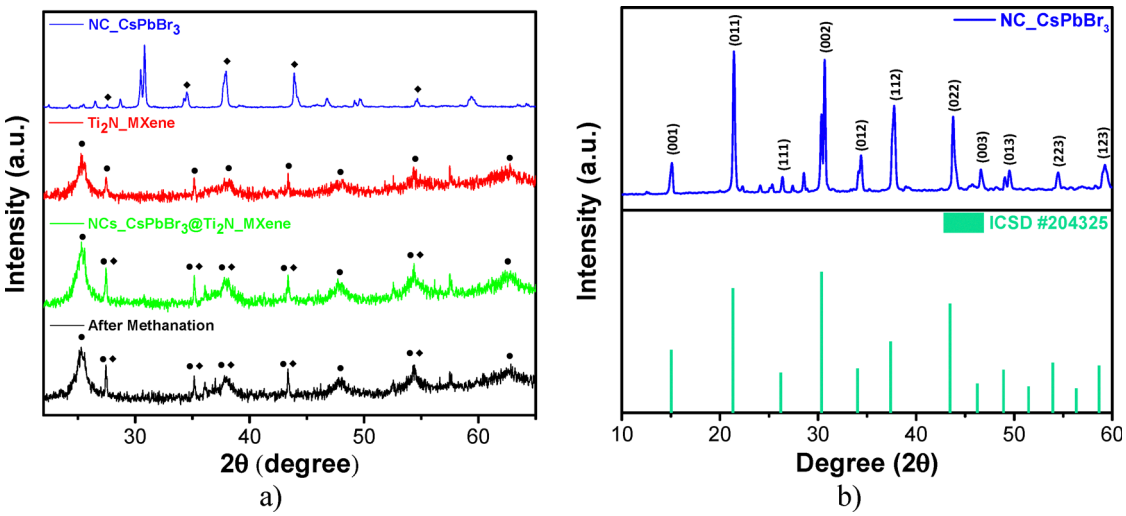

Fig. 1 (a) Comparative XRD patterns of $CsPbBr_3$ NCs (blue), POM–Ti_2N MXene (red), NCs@POM–Ti_2N before (green) and after the catalytic reaction (black), (b) $CsPbBr_3$ NCs compared with reference data from the ICSD #204325 data file.

confirmed from the DF STEM image in Fig. S6. This image showed that elements that form the perovskite particles are well dispersed and distributed homogenously over the support. A clearer image that shows the physical presence of perovskite NCs on the POM–Ti_2N support is shown in Fig. S7, from which we can estimate a loading of 5% per weight of NCs on the POM–Ti_2N MXene.

To elucidate the fine structure of the hybrid, HR-TEM images of NCs@POM–Ti_2N are presented in Fig. 2g and h. As shown in Fig. 2g, TiO_2 nanoparticles are uniformly anchored onto the Ti_2N MXene sheets, forming a surface-decorated[25] hybrid. This observation confirms that the partial surface transformation of Ti_2N into TiO_2 occurs during processing, yielding a coherent TiO_2/Ti_2N heterostructure.[26]

The distinct lattice fringes observed for both phases further verify the successful formation of the composite (Fig. 2h). Spacings of 3.50 Å and 2.70 Å, as well as 2.10 Å, correspond to the (101) planes of anatase TiO_2[26] and the $(01\bar{1}0)$ planes of Ti_2N,[27,28] respectively. In addition, the lattice fringes of 3.00 Å are assigned to the (200) planes of $CsPbBr_3$ nanocrystals,[29] indicating their favourable deposition across the entire TiO_2/Ti_2N MXene surface.

Interestingly, the Ti_2N nanosheets appear partially intercalated among the surface-grown TiO_2 nanoparticles, generating a textured template onto which $CsPbBr_3$ NCs are subsequently anchored. This morphological arrangement is entirely consistent with the structural model illustrated in Fig. 8a for NCs@POM–Ti_2N. Such an architecture provides an enlarged interfacial contact area, thereby facilitating efficient charge-carrier migration throughout the heterostructure.

The thermal stability of $CsPbBr_3$ and the POM–Ti_2N MXene was investigated using thermogravimetric analysis (TGA) (Fig. S8). The results indicate that the POM–Ti_2N MXene exhibits high thermal stability, showing only a small percentage of weight loss over the entire temperature range studied. In addition, $CsPbBr_3$ (NCs) shows a sharp weight loss around 600 °C, indicating thermal stability up to this temperature. All of the above indicates the stability of the materials under the catalytic conditions studied.

The surface change induced by the partial oxidation of M–Ti_2N produces profound changes in the optical absorption of the material. As shown in Fig. S9, when titanium nitride is present, the absorbance spans the UV region to the entire visible range. However, when oxidation occurs, its absorbance becomes significantly more prominent in the UV region up to 380 nm due to the appearance of TiO_2 domains on the M–Ti_2N structure. For the sake of comparison, diffuse reflectance UV-vis spectra of perovskite NCs, the POM–Ti_2N MXene, and the composite NCs@POM–Ti_2N are also plotted in Fig. 3. Herein, we can see the POM–Ti_2N MXene UV-vis spectra exhibiting a strong band absorption with an edge at 380 nm, characteristic of TiO_2 absorption. In the case of $CsPbBr_3$ NCs, they display characteristic UV-vis absorption within the wavelength range of $\lambda < 540$ nm. The UV-vis spectrum also verifies the formation of the composite NCs and POM–Ti_2N MXene as the supported material combines both absorptions, expanding the photophysical response of the initial POM–Ti_2N in the visible region.

The optical band gaps (E_g) of the synthesized materials were determined using UV-vis diffuse reflectance spectroscopy (DRS), analyzed through Tauc plot extrapolations (Fig. S10, SI).[30] The extracted band gap values were found to be 2.28 eV[31] for $CsPbBr_3$ NCs and 3.26 eV for POM–Ti_2N, respectively.

To further elucidate the superior optoelectronic behavior of the perovskite material, the valence band edge positions (E_v^{NHE}) relative to the normal hydrogen electrode (NHE) were investigated using X-ray photoelectron spectroscopy (XPS).[32–34] The E_v^{NHE} values were calculated based on eqn (1):

$$E_v^{NHE} = E_v^f + \varphi_{sp} + E_0^{NHE} \quad (1)$$

where E_v^f is the Fermi level of the material determined from XPS measurements, φ_{sp} is the spectrometer work function

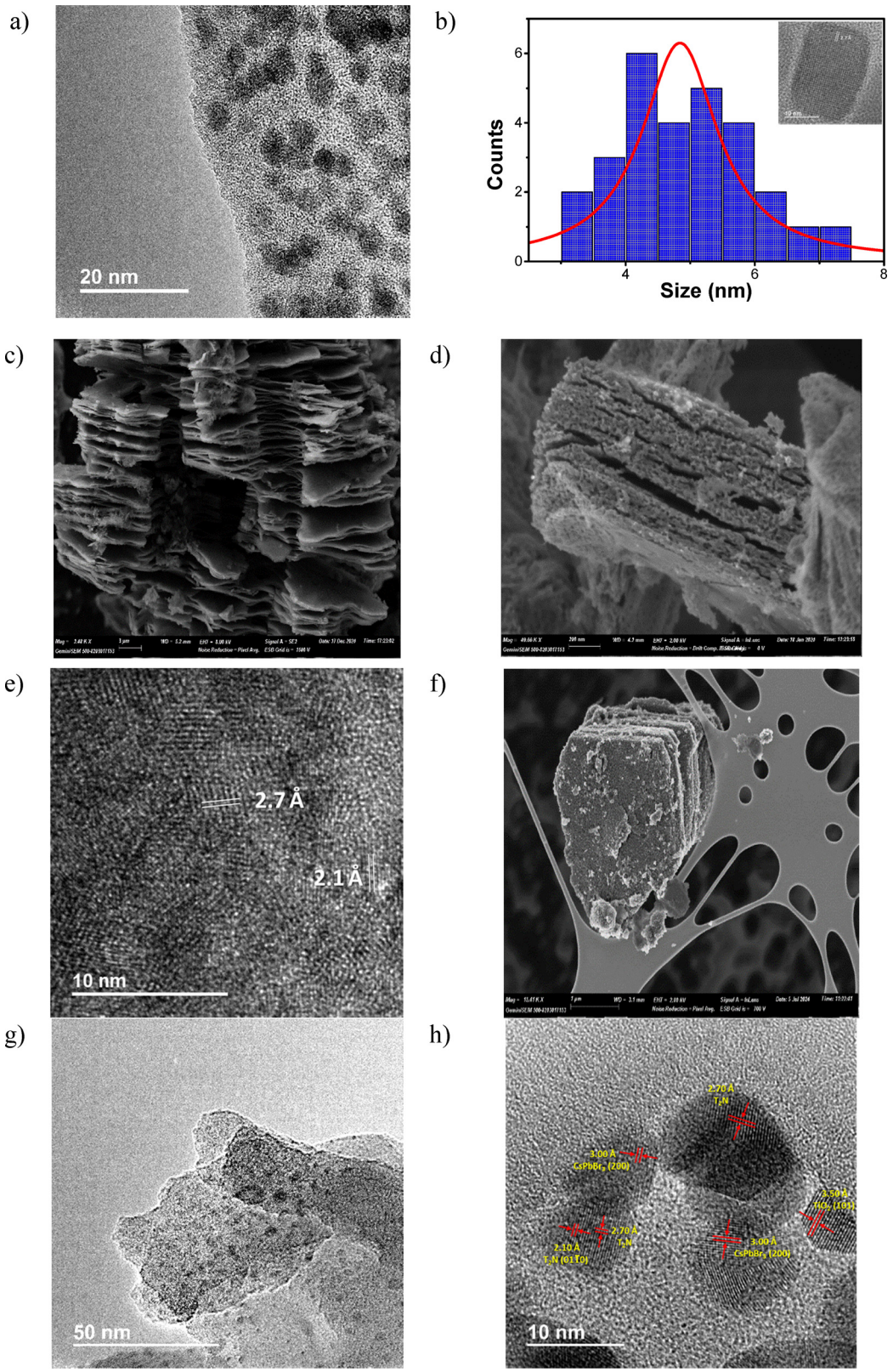

Fig. 2 (a) HR-TEM image showing the lead halide perovskite ($CsPbBr_3$) nanocrystals. (b) Histogram for the size distribution of the $CsPbBr_3$ NCs, the inset shows enlarged individual NCs, (c) HR-FESEM image of the Ti_2N MXene, (d) HR-FESEM picture of POM–Ti_2N, (e) HR-TEM of a layer of POM–T_2N with different interplanar distances, (f) HR-FESEM images of the composite NCs@POM–Ti_2N. (g) TEM image showing $CsPbBr_3$ NCs distributed across the Ti_2O/Ti_2N MXene. (h) Corresponding high-resolution (HR-TEM) image of NC@POM–Ti_2N displaying the lattice fringes assigned to anatase TiO_2 (3.50 Å, (101)), Ti_2N MXene (2.70 Å and 2.10 Å, (0110)), and $CsPbBr_3$ nanocrystals (3.00 Å, (200)), confirming the formation of the Ti_2O/Ti_2N heterostructure decorated with $CsPbBr_3$ NCs.

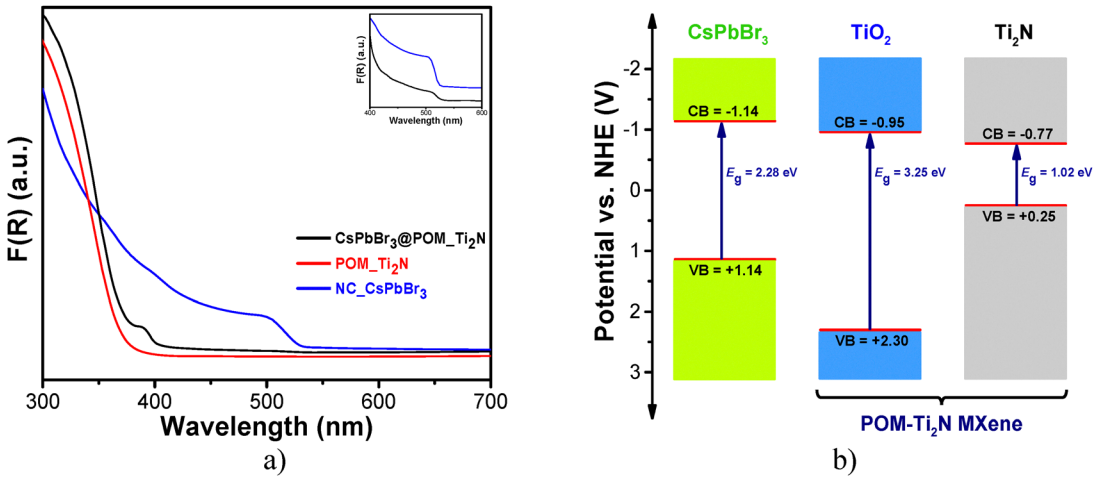

Fig. 3 (a) Diffuse reflectance UV-vis optical spectra of $CsPbBr_3$ NCs, the Ti_2N MXene and the supported material. The inset shows a magnification in the characteristic range of the $CsPbBr_3$ NCs absorption. (b) Schematic energy band level diagram of each component of the $CsPbBr_3$@POM–Ti_2N composite. The respective CB and VB values, as well as the optical band gaps (all in eV), are extracted from the XPS and UV-vis measurements respectively.

(4.244 eV), and E_0^{NHE} is the energy level of the standard hydrogen electrode relative to the vacuum level (−4.44 eV).

Based on the calculated valence band (VB) positions and the corresponding optical band gaps, the conduction band minimum (CB) energies were inferred for each material. The estimated VB potentials referenced to the NHE were 1.14 eV for $CsPbBr_3$ NCs and 2.30 eV for POM–Ti_2N, as shown in Fig. S11(a and b). Moreover, the CB values of $CsPbBr_3$ NCs and POM–Ti_2N are −1.14 and −0.96 eV, respectively. Regarding the POM–Ti_2N MXene material, we expect two distinct regions: an outer region corresponding to the partially oxidized Ti_2N MXene with TiO_x groups exhibiting electron-withdrawing behavior, and an inner region mainly of the Ti_2N MXene with a metallic character, which facilitates efficient electron extraction. Consequently, energy band diagrams were constructed, providing comprehensive insight into the electronic structure of the materials investigated (Fig. 3b).

With the aim to understand the mechanism of the catalytic process that occurs during the photo-thermal reaction, steady-state and lifetime emission were studied. The PL spectrum of the $CsPbBr_3$ NCs exhibits a strong emission peak at 530 nm; however, for the sample $CsPbBr_3$@POM–Ti_2N MXene, we observed a decrease in PL intensity along with a blue shift in the peak maximum to 513 nm. This shift to the blue can be attributed to the Burstein–Moss effect.[35] This effect is related to the change in carrier concentration caused by the electronic coupling between the perovskite nanocrystals and the MXene material. In addition, the decrease in emission intensity can be ascribed to the transfer of photogenerated carriers between the $CsPbBr_3$ NCs and the POM–Ti_2N MXene.[36]

Time-resolved fluorescence spectroscopy (Fig. 4) was used to investigate the lifetime emission of pure $CsPbBr_3$ NCs and the supported $CsPbBr_3$@POM–Ti_2N MXene catalyst. The best

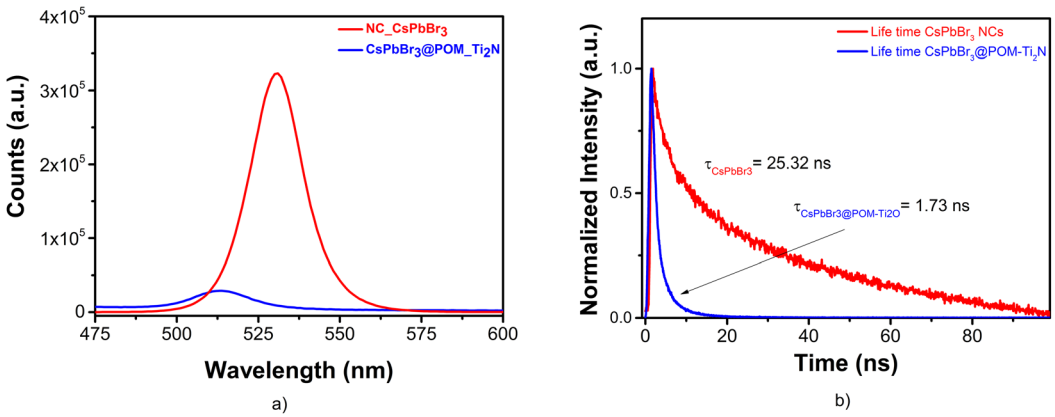

Fig. 4 (a) Photoluminescence spectra (λ_{ex} = 405 nm) of $CsPbBr_3$ nanoparticles (red line) and the $CsPbBr_3$@POM Ti_2N MXene catalyst (blue line). (b) Lifetime measurements registered at 530 and 513 nm under room conditions of $CsPbBr_3$ nanoparticles (blue line) and the $CsPbBr_3$@POM Ti_2N MXene catalyst (red line) respectively. The PL decay lifetimes were calculated from the best fitting to a biexponential decay model ($y = A_1 \cdot e^{-t/\tau 1} + A_2 \cdot e^{-t/\tau 2}$), where A_1 and A_2 correspond to the amplitudes and τ_1 and τ_2 are the lifetimes of each component. The average lifetime was calculated using the formula: $\tau_{average} = A_1 \cdot \tau_1^2 + A_2 \cdot \tau_2^2 / A_1 \cdot \tau_1 + A_2 \cdot \tau_2$.

fitting corresponds to a biexponential decay model, where the short lifetime is attributed to nonradiative recombination of electron–hole pairs and surface trap states and the long lifetime to the radiative recombination.[37,38]

The emission lifetime of the $CsPbBr_3$@POM Ti_2N MXene (τ_{ave} = 1.73 ns) was relatively shorter than that of the corresponding $CsPbBr_3$ nanoparticles (τ_{ave} = 25.32 ns). This difference in the emission lifetime between both materials indicates the emergence of a nonradiative pathway from the significant electronic interaction between $CsPbBr_3$ nanoparticles and the partially oxidized MXene.[18] This provides an alternative interfacial pathway for the excited electrons of $CsPbBr_3$ to transfer to the oxidized MXene and relax non-radiatively, allowing them to participate in the catalytic reaction.[35,39]

X-ray photoelectron spectroscopy (XPS) measurements were conducted to determine the chemical states of lead (Pb), bromine (Br), cesium (Cs), titanium (Ti), nitrogen (N) and oxygen (O) in the $CsPbBr_3$ NCs, POM–Ti_2N, and NCs@POM–Ti_2N samples (Fig. S12–S14 show the full survey scans). Fig. S12 displays the XPS core spectra of Cs 3d, Pb 4f, and Br 3d states, respectively, calibrated using the adventitious C 1s peak set to a binding energy (BE) of 284.8 eV.[40] In the case of $CsPbBr_3$ NCs, the BE peaks for Cs 3d at 724.0 and 738.0 eV correspond to the Cs $3d_{5/2}$ and Cs $3d_{3/2}$ signals (Fig. 5a), while the Pb 4f spectrum shows two peaks at 138.0 and 142.9 eV, attributed to the Pb $4f_{7/2}$ and Pb $4f_{5/2}$ levels respectively, of the Pb^{2+} state, consistent with previous literature reports[41,42] (Fig. 5b). Additionally, two Br 3d peaks are observed at 67.9 and 69.0 eV, corresponding to Br $3d_{5/2}$ and Br $3d_{3/2}$ contributions[43,44] (Fig. 5c). Further examination of the Ti 2p spectrum for the NCs@POM–Ti_2N composite reveals that the Ti $2p_{3/2}$ and Ti $2p_{1/2}$ levels corresponding to Ti–N in POM–Ti_2N appear at BE values of 458.5 and 464.2 eV, respectively. The Ti $2p_{3/2}$ and Ti $2p_{1/2}$ levels associated with Ti–O bonds characterize the POM–Ti_2N MXene, with various oxidation states from Ti^{2+} to Ti^{4+} presenting at BE values around 455.7–459.8 and 461–466 eV, respectively[45,46] (Fig. 5d).

Further evidence of the formation of the composite NCs@POM–Ti_2N is found in the XPS spectrum shown in Fig. 5, which shows the elemental XPS signals of $CsPbBr_3$ and the POM–Ti_2N MXene before and after the formation of the composite. Due to the effective formation of an interface between perovskites and the POM–Ti_2N MXene, subtle shifts in the Pb, Br, Ti, and N peak positions are observed, as shown below. Specifically, the binding energies for Pb 4f and Br 3d in the NCs@POM–Ti_2N composite shift towards more positive values, indicating a reduction in electron density on $CsPbBr_3$.[47] Conversely, the binding energies assigned to Ti 2p and N 1s (from Ti–N bonding) exhibit a negative shift, suggesting an increase in electron density on the POM–Ti_2N MXene particles (Fig. 5d and e).[48] The Ti 2p spectrum of the NCs@POM–Ti_2N composite shows a clear shift of the main peak positions to lower BE values compared to the POM-Ti_2N MXene alone, indicating a chemical interaction between the perovskite nanocrystals and the POM–Ti_2N MXene structure.

In addition, despite partial oxidation of the nitride MXene, Ti–N bonds characteristic of titanium nitride predominate, as evidenced by Ti $2p_{3/2}$ and Ti $2p_{1/2}$ signals at binding energies of approximately 458.5 eV and 464.2 eV, respectively. Additionally, the presence of an N 1s signal around 399.5 eV confirms the continued existence of N–Ti bonds,[49,50] and the peak at 400.8 eV may be associated with nitrogen atoms in the Ti(N, O) oxynitride lattice (Fig. 5e).

These findings indicate that, although some surface oxidation occurs, forming TiO_2, the internal structure of POM–Ti_2N predominantly retains its titanium–nitride bonds, thus facilitating an effective electronic interaction with the $CsPbBr_3$ nanocrystals. In summary, all these observations support the notion of electronic interaction between the orbitals that form $CsPbBr_3$ NCs and the POM–Ti_2N MXene.

To investigate the reducibility and metal–support interactions within the hybrid, H_2 temperature-programmed reduction (H_2-TPR) measurements were conducted (Fig. 6a). Pure TiO_2 exhibits only a weak, broad reduction event centred at ~535 °C,[51] characteristic of kinetically hindered lattice-oxygen removal and indicative of strongly bound oxygen species with low surface mobility. A similar trend has been observed for TiO_2 nanosheets by other authors.[52] Conversely, the POM–Ti_2N composite exhibits a markedly different H_2 consumption behavior, revealing two pronounced low-temperature reduction peaks with maxima centered at 314 °C and 381 °C. The presence of these features at significantly lower temperatures reflects the formation of highly labile surface oxygen species generated at the Ti_2N/TiO_2 interface.[53] According to the reducibility criterion, where lower peak temperatures correspond to more weakly bonded oxygen species such as O^-/O^{2-},[54] these events confirm the emergence of readily accessible active oxygen centres not present in pristine TiO_2. This enhanced reducibility is attributed to a strong metal–support interaction (SMSI) between the almost conductive Ti_2N core and the ultrathin surface-oxidised TiO_2 shell.[55] The Ti_2N framework promotes electron donation, activating H_2 molecules and facilitating the formation of hydrides, which collectively weakens the surface Ti–O bonds and triggers stepwise reduction of the MXene surface. Concurrently, the high-temperature feature centred at ~530 °C originates from the reduction of oxidised TiO_2 moieties anchored on the POM surface, consistent with the consumption of more strongly bound lattice oxygen. Taken together, these redox characteristics demonstrate that the POM–Ti_2N hybrid possesses substantially improved oxygen lability and electronic coupling compared to pristine TiO_2. Such behaviour is essential for catalytic activation, as the generation of easily reducible oxygen species and the formation of a robust Ti_2N–TiO_2 heterojunction provide the active environment required for efficient H_2 dissociation, CO_2 adsorption, and subsequent photothermal reduction to CO and CH_4.

Furthermore, the CO_2 adsorption behaviour of POM–Ti_2N and TiO_2 was further examined by CO_2 temperature-programmed desorption (CO_2-TPD), as illustrated in Fig. 6b. POM–Ti_2N and TiO_2 exhibit a desorption peak in the low-temperature region (~105 °C),[56] which can be attributed to physisorbed CO_2 weakly interacting with surface hydroxyl groups. In the case of TiO_2, this low-temperature feature dominates the profile, indicating a

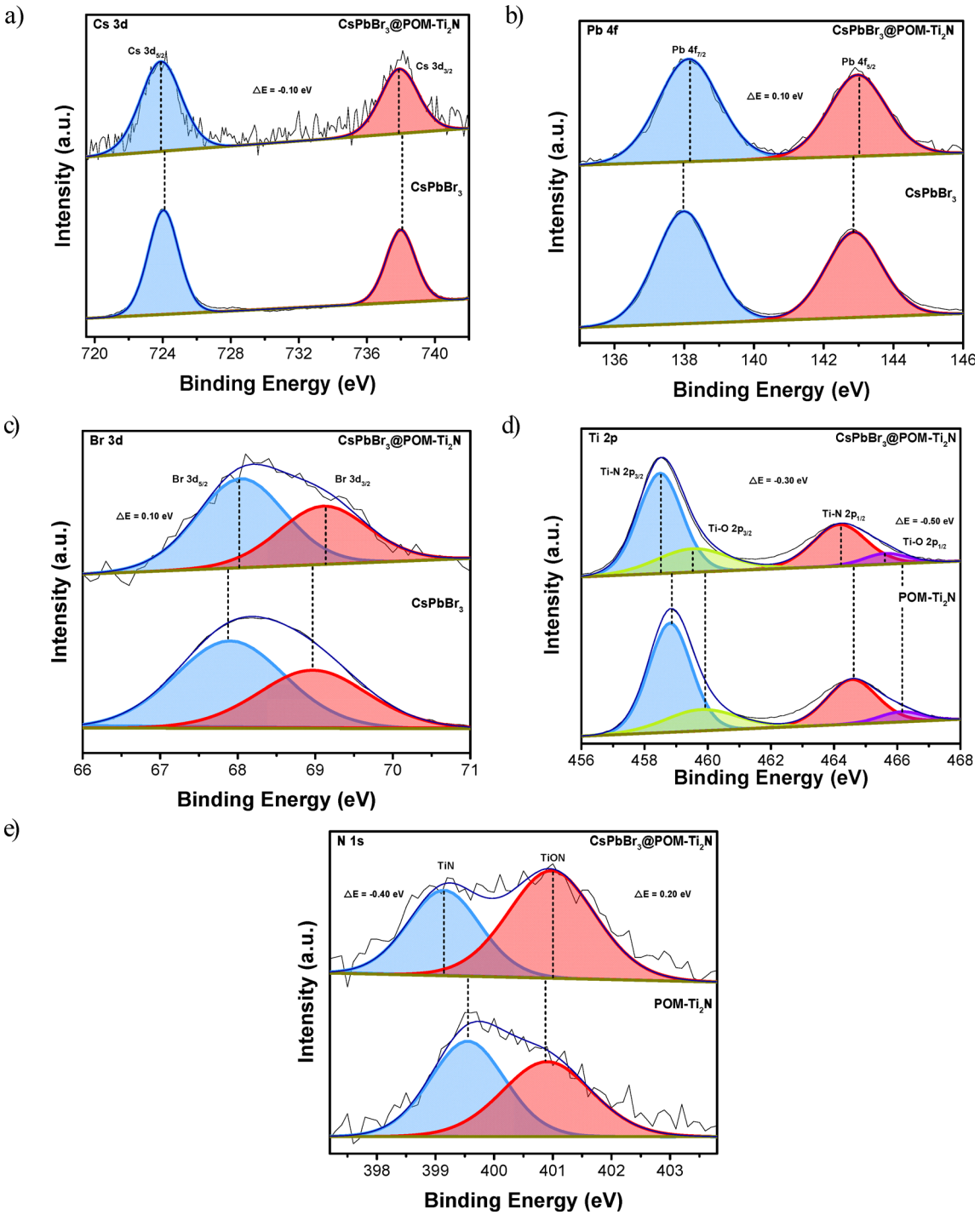

Fig. 5 XPS spectra of $CsPbBr_3$ NCs, POM–Ti_2N (below), and NCs@POM–Ti_2N composites (top): (a) Cs 3d spectra, (b) Pb 4f spectra, (c) Br 3d spectra, (d) Ti 2p spectra, and (e) N 1s spectra.

limited population of strongly adsorbed carbonate species.[57] In contrast, POM–Ti_2N displays a markedly enhanced desorption signal extending into the high-temperature region (350–700 °C), with a pronounced maximum centred at approximately 525 °C. This peak reflects the formation of strongly bound carbonate species, resulting from the interaction of CO_2 with basic surface sites generated during the formation of the TiO_2 moieties within the POM–Ti_2N heterostructure. The significantly increased desorption intensity suggests an enlarged density of active sites capable of stabilising chemisorbed CO_2 species. These results collectively indicate that the incorporation of Ti_2N and its partial oxidation to TiO_2 enhance both the strength and capacity of CO_2 adsorption.

Periodic DFT calculations were performed with VASP (PAW-PBE including dispersion corrections;[58,59] full computational

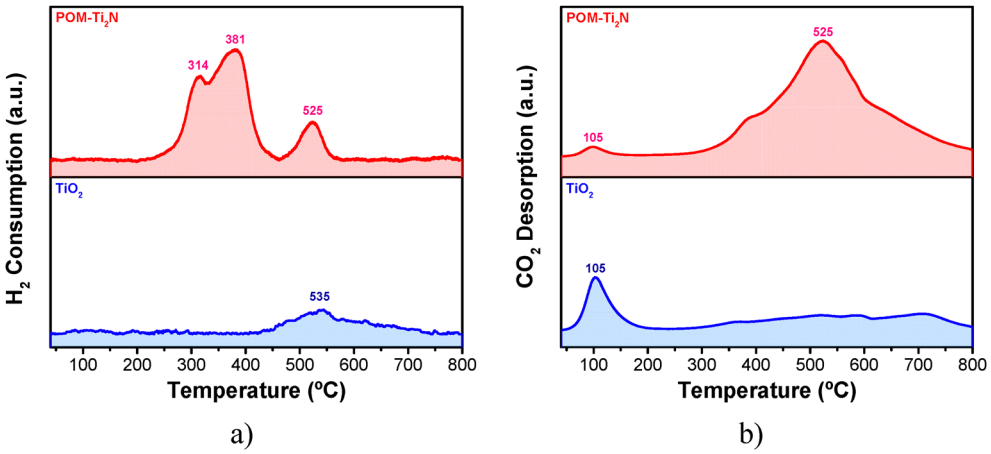

Fig. 6 (a) H_2-TPR analysis profiles of the tested materials: POM–Ti_2N (red line) and TiO_2 (blue line). (b) CO_2-TPD profiles obtained on POM–Ti_2N (red line) and TiO_2 (blue line) materials. In both studies, the ramp rate was 10 °C min^{-1}.

details are provided in the SI) on three representative Ti-based supports designed to mimic the POM–Ti_2N composite: a Ti_2N MXene monolayer (conductive nitride core), a rock-salt TiN(100) slab (nitride surface), and rutile TiO_2 (110) surfaces with and without a surface oxygen vacancy, V_O (partially oxidized TiO_2/TiO_x domains) (Fig. S15). CO_2 and H_2 were individually adsorbed at low coverage on each model, exploring several initial geometries. Among these, Ti_2N exhibited the largest thermodynamic affinity for CO_2 (E_{ads} = −3.32 eV),[60,61] whereas stoichiometric TiO_2(110) bound to CO_2 only weakly (E_{ads} = −0.10 eV), in line with previous DFT and surface-science studies.[62,63] Introducing a surface oxygen vacancy on TiO_2(110) markedly strengthened CO_2 adsorption (E_{ads} = −1.11 eV) and led to bent, vacancy-anchored configurations, consistent with the enhanced reactivity of defective rutile surfaces.[64–66] In contrast, molecular H_2 adsorption was found to be very weak on all Ti-based supports ($|E_{ads}(H_2)| \leq 0.05$ eV), while an artificially initialized, dissociated H_2 state on Ti_2N was strongly stabilized (E_{ads} = −7.57 eV per H_2), indicating that nitride sites act as a deep thermodynamic sink for atomic hydrogen rather than as strong chemisorption sites for molecular H_2.[67] Taken together with the H_2-TPR and CO_2-TPD data, these DFT trends support a bifunctional picture in which oxygen-deficient TiO_2/TiO_x regions and TiO_2/Ti_2N interfacial sites provide the main CO_2-binding and activation centres, whereas the TiN/Ti_2N scaffold supplies electronic/photothermal conductivity and preferentially stabilizes dissociated hydrogen species, as described in detail in the DFT analysis (see SI).

Catalytic activity of the NCs@POM–Ti_2N material

First, the catalytic activity of NCs@POM–Ti_2N was studied at temperatures ranging between 160 and 250 °C, either in the dark (thermal catalysis) or under light irradiation (photothermal catalysis). Fig. 7 and Fig. S16 and S17 summarize the catalytic results obtained under light and dark conditions. In both cases, under light or dark conditions, at low temperatures

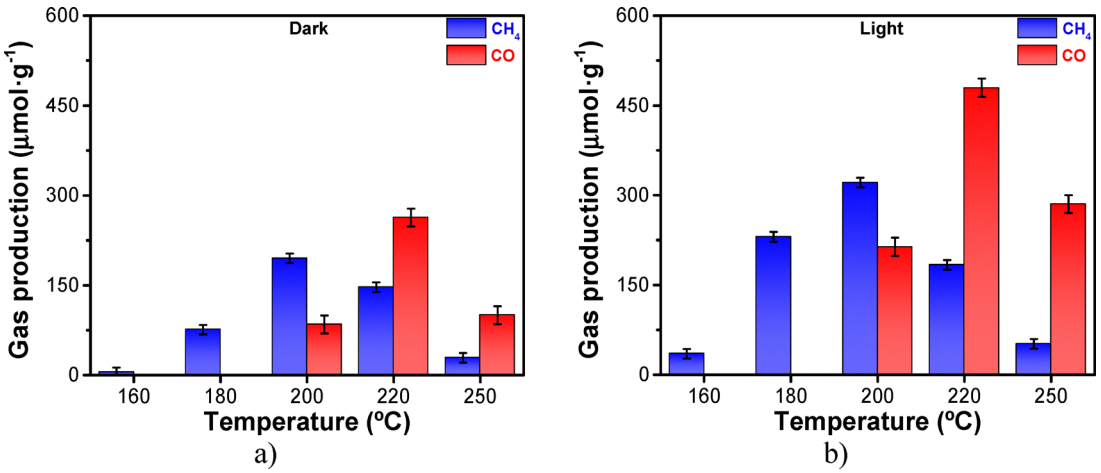

Fig. 7 Photocatalytic activity of $CsPbBr_3$(5 wt%)@POM–Ti_2N MXene under different conditions of temperature (a) in the dark and (b) under light irradiation. Reaction conditions: $CsPbBr_3$(5 wt%)@POM–Ti_2N MXene (10 mg), P_{H_2} = 1.2 bar, P_{CO_2} = 0.3 bar, at 23 h reaction time, simulated sunlight irradiation (226 mW cm^{-2}), and temperature as indicated.

selectivity towards CH_4 is 100% but as temperature increases selectivity shifts to CO. Additionally, maximum conversion is achieved above 200 °C, whereas at 250 °C the activity drops. This fact may be due to changes happening on the support as the colour of POM–Ti_2N shifted from light grey to dark grey at these temperatures. On the other hand, as shown in Fig. 7, under light irradiation production of CO_2-derived products is always higher compared to dark conditions. These differences in the catalytic activity indicate that light effectively assists the CO_2 conversion reaction in NCs@POM–Ti_2N.

A deeper analysis of catalytic data summarized in Table 1 brings further arguments for the photo-thermal catalytic pathway, especially, which is more evident at lower temperatures. A comparison of CO_2 conversion or CH_4 production at temperatures of 160 °C or 180 °C leads to conversions 5 to 4-fold higher when photo-thermal conditions are applied. Interestingly, both thermal and photothermal conditions share similar trends displaying higher conversions at 220 °C; in both cases, CO production starts at 200 °C and has a Gaussian plot in which 220 °C seems to be the optimum temperature conditions. It seems that at higher temperatures than 180 °C desorption of reaction intermediates is favored and the complete hydrogenation of CO_2 to CH_4 is difficult.

Table 1 Comparison of the CH_4 and CO selectivity of $CsPbBr_3$(5 wt %)@POM–Ti_2N MXene at different temperatures and under different conditions (dark or light)

$T_{reaction}$ (°C)	Conditions	Selectivity for CH_4 (%)	Selectivity for CO (%)
160	Dark	100	0
	Light	100	0
180	Dark	100	0
	Light	100	0
200	Dark	70	30
	Light	60	40
220	Dark	36	64
	Light	28	72
250	Dark	22	78
	Light	15	85

For comparison, we studied the photo-thermal activity for CO_2 reduction using $CsPbBr_3$ nanocrystals and $CsPbBr_3$@POM–Ti_2N MXene at 200 °C. (Fig. 8). As can be seen, our $CsPbBr_3$@POM–Ti_2N catalyst presents the highest activity for CH_4 production compared to pristine $CsPbBr_3$ NCs or POM–Ti_2N MXene alone. In fact, while the components of the composite $CsPbBr_3$ and M–Ti_2N MXene are not as active as the pristine POM–Ti_2N we assume that the catalytically active sites are present in the oxidized side of POM–Ti_2N. (Fig. 8a) However, selectivity changes occurred when POM–Ti_2N was loaded with the perovskite due to the suppression of CO production and a change in selectivity towards CH_4. This indicates a synergistic effect between both materials when they form a combined material.

In addition, the recyclability of $CsPbBr_3$@POM–Ti_2N MXene was evaluated over five consecutive cycles under identical reaction conditions, as illustrated in Fig. 8b. The results indicate a stable CH_4 production yield for the first three cycles (only a 3% reduction in activity per cycle), suggesting desirable photostability of the catalyst, even with each cycle lasting 23 hours. Interestingly, while CH_4 remained the primary product, CO was observed as a byproduct of the reaction. We attribute this emergent CO formation to surface restructuring and the gradual alteration of active sites, likely due to subtle changes in the surface composition or morphology of $CsPbBr_3$@POM–Ti_2N during the initial reaction cycle. This shift in selectivity, with CO generation emerging, may be explained by changes in the binding and activation of CO_2 at newly exposed or modified active sites on the catalyst surface. This argument is reinforced by XPS data shown in Fig. 5 which reveal the electronic polarization in Cs and Ti atoms after the formation of $CsPbBr_3$@POM–Ti_2N, suggesting that perovskite NCs are not randomly deposited, if not interacting somehow. Photocatalytic CO_2 reduction involves a series of complex, multi-step processes, including light absorption, charge separation, reactant adsorption, and catalytic reduction at active sites.[68] Minor modifications in any of these

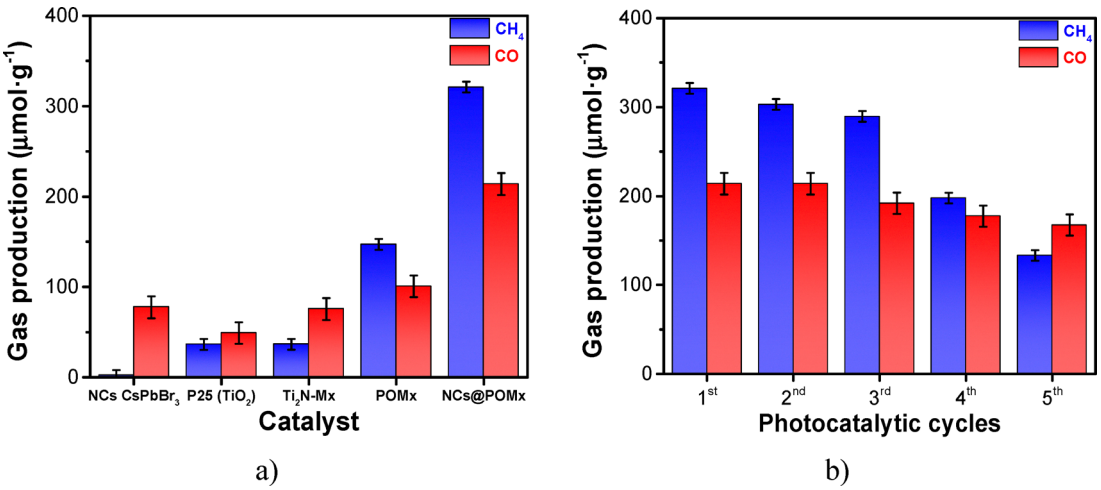

Fig. 8 (a) Comparison of photocatalytic activity for different samples. (b) Recycling of the photocatalyst $CsPbBr_3$(5 wt%)@POM–Ti_2N MXene. Reaction conditions: photocatalyst (10 mg), P_{H_2} = 1.2 bar, P_{CO_2} = 0.3 bar, at 23 h reaction time, simulated sunlight irradiation (226 mW cm^{-2}), and 200 °C.

steps, particularly in the structure of surface-active sites, can significantly impact product selectivity. In this case, the MXene support likely plays a dual role: enhancing electron–hole separation and simultaneously protecting $CsPbBr_3$ nanocrystals from rapid degradation, as confirmed by the absence of notable changes in XRD patterns (Fig. 1, black line) and consistent XPS spectra. Nevertheless, with continued cycling, slight restructuring of the surface may expose new catalytic sites that favor CO production. By the fourth cycle, a reduction of approximately 30% in CH_4 yield was observed, possibly due to gradual surface degradation or partial deactivation of active sites, while CO production remained stable. This indicates that, despite a decrease in CH_4 yield, the modified surface continues to facilitate CO_2 reduction to CO, suggesting persistent reactivity at specific catalytic sites that favor CO production over CH_4. In fact, while $CsPbBr_3$@POM–Ti_2N has higher selectivity towards CH_4, its individual components (the M–Ti_2N MXene, the POM–Ti_2N MXene, and $CsPbBr_3$ nanocrystals) are also selective to CO. This change in catalytic activity agrees with superficial chemicophysical changes on the POM–Ti_2N surface. This matches with the observation made using XPS in terms of electronic densities of atomic elements that compose $CsPbBr_3$ NCs and POM–Ti_2N. These findings underscore the importance of optimizing both the initial surface properties and long-term stability of active sites to maintain selective CO_2 photoreduction over extended reaction cycles.

Proposed mechanism (photocatalytic CO_2 reduction)

According to XPS and UV-vis measurements, the energy alignments of the CB and VB of $CsPbBr_3$ NCs, POM–Ti_2N, and $CsPbBr_3$@POM–Ti_2N were calculated. From a thermodynamic point of view, the reduction of CO_2 to CO and CH_4 occurs in all cases, see Fig. 9b. However, CO_2 conversion increases considerably in the case of the $CsPbBr_3$@POM-Ti_2N composite, especially upon UV-vis light exposure. This fact, plus the intrinsic heterojunction morphology of the composite (see Fig. 9a), suggests that photogenerated electrons can flow from the conduction band (CB) of the perovskite to the CB of the TiO_2 layer that eventually will pass to Ti_2N, thus inducing effective charge separation enabled by a type II heterojunction formed between the $CsPbBr_3$ NCs and the POM-Ti_2N MXene structure. Additionally, the difference in potential between the two materials generates an internal electric field (IEF) that further enhances charge separation and transfer efficiency.[69] The direction of the IEF is shown by XPS results (Fig. 5).

The TiO_2 layer also reduces direct recombination between the perovskite and the MXene, forming an additional small electric field that promotes electron flow into the MXene and avoids recombination. The introduction of such an interlayer to reduce direct recombination is a well-known strategy in the field of dye-sensitized solar cells (DSSCs) and hybrid solar cells.[70,71]

Thus, these electrons that are injected into the MXene can reduce CO_2 into either CO or CH_4 through multielectron transfer pathways:[72]

$$CO_2 + 2H^+ + 2e^- \rightarrow CO + H_2O \quad (E^0_{redox} = -0.53\ V) \qquad (2)$$

$$CO_2 + 8H^+ + 8e^- \rightarrow CH_4 + 2H_2O \quad (E^0_{redox} = -0.24\ V) \qquad (3)$$

Moreover, these reactions proceed concurrently, with their predominance governed by the interplay between thermodynamic feasibility and kinetic accessibility. Thermodynamically,

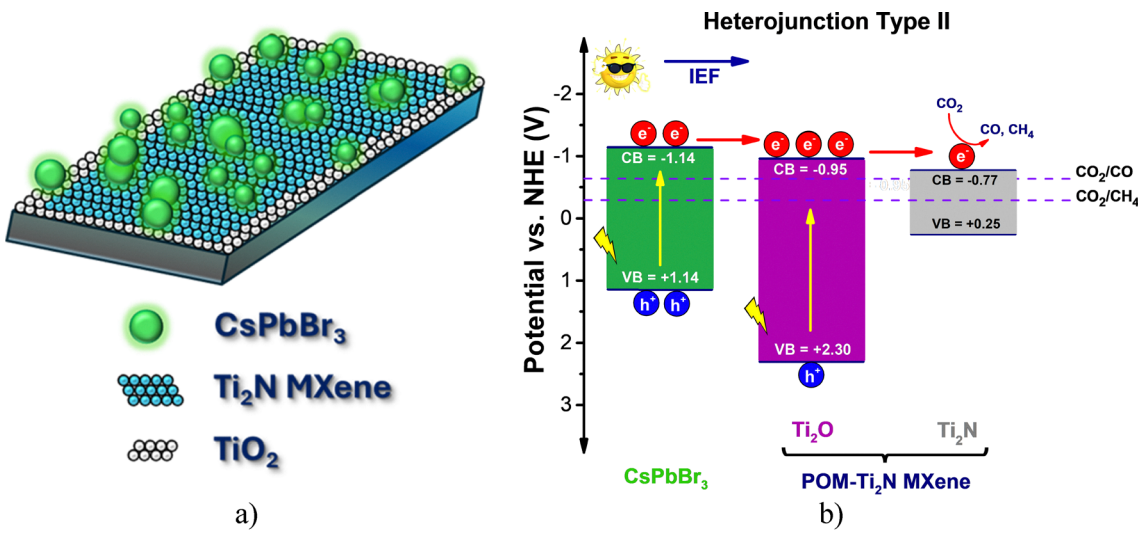

1. Upon illumination, the perovskite absorbs photons, generating electron-hole pairs.
2. Internal electric fields (IEF) push electrons toward TiO_2 and then to MXene.
3. Electrons accumulate at the MXene surface, where they reduce CO_2 to CO and CH_4.

Fig. 9 (a) The schematic diagram of the $CsPbBr_3$@POM-Ti_2N composite. (b) Diagram of CH_4 and CO production by the $CsPbBr_3$@POM-Ti_2N composite system under sunlight irradiation and charge migration and separation. (1) Upon illumination, the perovskite absorbs photons, generating electron–hole pairs. (2) Internal electric fields (IEF) push electrons toward TiO_2 and then to the MXene. (3) Electrons accumulate at the MXene surface, where they reduce CO_2 to CO and CH_4.

the formation of CH_4 is favored; however, kinetically, CO production is more accessible as it requires fewer electrons ($2e^-$ *vs.* $8e^-$ for CH_4). Experimental data from Table 1 and Fig. 7 confirm this duality. At lower temperatures (160–180 °C), CH_4 selectivity remains at 100%, indicating a thermodynamically driven process. However, as the temperature increases (200–250 °C), a significant shift in selectivity toward CO is observed, dropping CH_4 selectivity to 15% under illumination at 250 °C. These results suggest that at higher reaction temperatures, kinetic factors increasingly govern product distribution.

Therefore, the temperature-dependent behavior observed in the $CsPbBr_3$@POM-Ti_2N composite under light irradiation illustrates a nuanced balance between thermodynamics and kinetics.[73]

In summary, the superior photocatalytic activity of $CsPbBr_3$@POM-Ti_2N can be attributed to several synergistic factors. First, the composite exhibits enhanced light absorption across the visible spectrum compared to the individual components (Fig. 8a), generating more charge carriers. Second, the heterojunction architecture suppresses electron–hole recombination, thereby ensuring greater availability of charge carriers for surface redox reactions. Lastly, the 2D/0D structural configuration—where zero-dimensional $CsPbBr_3$ NCs are uniformly distributed over a two-dimensional layers of POM–Ti_2N support—maximizes the active surface area and facilitates efficient interfacial charge migration (Fig. 9).

3. Conclusions

In conclusion, this study highlights the successful synthesis and performance of a novel hybrid heterojunction composed of $CsPbBr_3$ nanocrystals supported on a partially oxidized Ti_2N MXene (POM-Ti_2N), specifically engineered for efficient photothermal CO_2 conversion into CH_4 and CO. Preparation of the hybrid material was achieved by simple ultrasonic impregnation, enabling the uniform deposition of $CsPbBr_3$ NCs onto the surface of the 2D POM–Ti_2N sheets. The partial oxidation of Ti_2N was fundamental to introducing oxygen-containing functional groups, which improved surface hydrophilicity and provided anchoring sites for the nanocrystals. This facilitated strong interfacial interactions, critical for enhancing the overall photocatalytic activity.

The proposed mechanism involves a synergistic interplay between light absorption, charge separation, thermodynamic, and kinetic effects. $CsPbBr_3$ NCs serve as efficient light harvesters due to their strong absorption in the visible range and excellent charge transport properties. Upon irradiation, electron–hole pairs are generated in the perovskite, with electrons being efficiently transferred to the POM-Ti_2N support. The partially oxidized MXene acts both as a photothermal catalyst and an electron sink, avoiding charge recombination to promote the catalytic reduction of CO_2, while simultaneously accelerating charge separation and transport. The presence of oxygen vacancies and various oxidation states from Ti^{2+} to Ti^{4+} on the POM–Ti_2N surface further facilitates CO_2 adsorption and activation, which are essential for driving the CH_4 and CO formation pathway with high selectivity.

In terms of recyclability, the hybrid catalyst demonstrated excellent structural integrity, maintaining its catalytic activity over multiple reaction cycles. Post-reaction analyses showed minimal degradation of the $CsPbBr_3$ NCs, retaining the interfacial architecture and confirming the robustness of the catalyst under operational conditions. Overall, the $CsPbBr_3$@POM–Ti_2N hybrid catalyst demonstrates a promising strategy for the design of stable and highly active photocatalysts, combining the tunable optoelectronic properties of perovskite NCs with the multifunctionality of 2D MXenes. The enhancement in CH_4 and CO production under light-driven conditions underscores the potential of this hybrid catalyst in advancing solar-to-fuel technologies.

Conflicts of interest

There are no conflicts to declare.

Data availability

The data supporting the results of this study are available from the corresponding author upon reasonable request.

Additional supporting information can be found online in the supplementary information (SI). Supplementary information is available. See DOI: https://doi.org/10.1039/d5ma01122a.

Acknowledgements

This research was funded by the Spanish Ministry of Science and Innovation through MCIN/AEI/10.13039/501100011033/ and ''FEDER a way of making Europe'' and the Severo Ochoa Centre of Excellence program (CEX2021-001230-S). K. M. acknowledges the PRE2022-104119 grant for the project ''Catalytic processes: catalysis for energy and process intensification by applying instrumental tools to monitor chemical processes.'' P. A. received funding from the PID2021-123163OB-I00 grant. H. G. B. was supported by the RYC2022-037287-I grant, PAID-06-23. Also, this research leading to these results has received funding from the European Union's Horizon Europe research and innovation programme (Project DAM4CO2, Double-Active Membranes for a sustainable CO_2 cycle; HORIZON-EIC-2022-PATHFINDERCHALLENGES-01-Number: 101115488). We thank the technical team at the Instituto de Tecnología Química (ITQ) for their support in facilitating the characterization.

References

1 X. Jiao, K. Zheng, L. Liang, X. Li, Y. Sun and Y. Xie, Fundamentals and Challenges of Ultrathin 2D Photocatalysts in Boosting CO2 Photoreduction, *Chem. Soc. Rev.*, 2020, **49**(18), 6592–6604, DOI: 10.1039/D0CS00332H.

2 G. Liao, G. Ding, B. Yang and C. Li, Challenges in Photocatalytic Carbon Dioxide Reduction, *Precis. Chem.*, 2024,

2(2), 49–56, DOI: 10.1021/PRECHEM.3C00112/ASSET/IMAGES/LARGE/PC3C00112_0004.JPEG.

3 J. Yu, A. Muhetaer, Q. Li and D. Xu, Solar Energy-Driven Reverse Water Gas Shift Reaction: Photothermal Effect, Photoelectric Activation and Selectivity Regulation, *Small*, 2024, **20**(42), 2402952, DOI: 10.1002/SMLL.202402952.

4 Y. Zhang, L. Ma, T. Wang and X. Li, MnO2 Coated Fe2O3 Spindles Designed for Production of C5+ Hydrocarbons in Fischer–Tropsch Synthesis, *Fuel*, 2016, **177**, 197–205, DOI: 10.1016/J.FUEL.2016.03.023.

5 P. Liu, Z. Huang, X. Gao, X. Hong, J. Zhu, G. Wang, Y. Wu, J. Zeng and X. Zheng, Synergy between Palladium Single Atoms and Nanoparticles via Hydrogen Spillover for Enhancing CO_2 Photoreduction to CH_4, *Adv. Mater.*, 2022, **34**(16), 2200057, DOI: 10.1002/ADMA.202200057.

6 N. D. M. Ridzuan, M. S. Shaharun, M. A. Anawar and I. Ud-Din, Ni-Based Catalyst for Carbon Dioxide Methanation: A Review on Performance and Progress, *Catal.*, 2022, **12**(5), 469, DOI: 10.3390/CATAL12050469.

7 S. Carenco, A. Tuxen, M. Chintapalli, E. Pach, C. Escudero, T. D. Ewers, P. Jiang, F. Borondics, G. Thornton, A. P. Alivisatos, H. Bluhm, J. Guo and M. Salmeron, Dealloying of Cobalt from CuCo Nanoparticles under Syngas Exposure, *J. Phys. Chem. C*, 2013, **117**(12), 6259–6266, DOI: 10.1021/JP4000297/SUPPL_FILE/JP4000297_SI_001.PDF.

8 S. Xiao, L. Wang, Y. Tang, Z. Yang, H. Wang, C. Guo, T. Zhao, Y. Jiang, X. Wen and F. Wang, Interfacial Structure Engineering Enhances Photo-Thermal CO2 Hydrogenation over Ni-CeO2 Nanocomposites, *Chem Catal.*, 2025, **5**(7), 101361, DOI: 10.1016/J.CHECAT.2025.101361.

9 Y. Tang, H. Wang, C. Guo, L. Wang, T. Zhao, S. Xiao, J. Liu, Y. Jiang, Y. Zhao, X. D. Wen and F. Wang, Synergies Between Atomically Dispersed Ru Single Atoms and Nanoparticles on CeAlOx for Enhanced Photo-Thermal Catalytic CO2 Hydrogenation, *Adv. Mater.*, 2025, e12793, DOI: 10.1002/ADMA.202512793;PAGE:STRING:ARTICLE/CHAPTER.

10 X. Li, C. Wang and J. Tang, Methane Transformation by Photocatalysis, *Nat. Rev. Mater.*, 2022, **7**(8), 617–632, DOI: 10.1038/s41578-022-00422-3.

11 T. Luo, L. Gilmanova and S. Kaskel, Advances of MOFs and COFs for Photocatalytic CO2 Reduction, H2 Evolution and Organic Redox Transformations, *Coord. Chem. Rev.*, 2023, **490**, 215210, DOI: 10.1016/J.CCR.2023.215210.

12 P. Wang, F. Yang, J. Qu, Y. Cai, X. Yang, C. M. Li and J. Hu, Recent Advances and Challenges in Efficient Selective Photocatalytic CO2 Methanation, *Small*, 2024, **20**(32), 2400700, DOI: 10.1002/SMLL.202400700.

13 Z. Shang, X. Feng, G. Chen, R. Qin and Y. Han, Recent Advances on Single-Atom Catalysts for Photocatalytic CO2 Reduction, *Small*, 2023, **19**(48), 2304975, DOI: 10.1002/SMLL.202304975.

14 S. Ullah, J. Wang, P. Yang, L. Liu, S. E. Yang, T. Xia, H. Guo and Y. Chen, All-Inorganic CsPbBr 3 Perovskite: A Promising Choice for Photovoltaics, *Mater. Adv.*, 2021, **2**(2), 646–683, DOI: 10.1039/D0MA00866D.

15 Y. H. Chen, J. K. Ye, Y. J. Chang, T. W. Liu, Y. H. Chuang, W. R. Liu, S. H. Liu and Y. C. Pu, Mechanisms behind Photocatalytic CO2 Reduction by CsPbBr3 Perovskite-Graphene-Based Nanoheterostructures, *Appl. Catal., B*, 2021, **284**, 119751, DOI: 10.1016/J.APCATB.2020.119751.

16 X. Wang, J. He, X. Chen, B. Ma and M. Zhu, Metal Halide Perovskites for Photocatalytic CO2 Reduction: An Overview and Prospects, *Coord. Chem. Rev.*, 2023, **482**, 215076.

17 X. Li, J. Liu, G. Jiang, X. Lin, J. Wang and Z. Li, Self-Supported CsPbBr3/Ti3C2Tx MXene Aerogels towards Efficient Photocatalytic CO2 Reduction, *J. Colloid Interface Sci.*, 2023, **643**, 174–182, DOI: 10.1016/J.JCIS.2023.04.015.

18 H. Pazniak, I. A. Plugin, M. J. Loes, T. M. Inerbaev, I. N. Burmistrov, M. Gorshenkov, J. Polcak, A. S. Varezhnikov, M. Sommer, D. V. Kuznetsov, M. Bruns, F. S. Fedorov, N. S. Vorobeva, A. Sinitskii and V. V. Sysoev, Partially Oxidized Ti_3C_2Tx MXenes for Fast and Selective Detection of Organic Vapors at Part-per-Million Concentrations, *ACS Appl. Nano Mater.*, 2020, **3**(4), 3195–3204, DOI: 10.1021/ACSANM.9B02223/ASSET/IMAGES/MEDIUM/AN9B02223_M001.GIF.

19 H. Wang, R. Peng, Z. D. Hood, M. Naguib, S. P. Adhikari and Z. Wu, Titania Composites with 2 D Transition Metal Carbides as Photocatalysts for Hydrogen Production under Visible-Light Irradiation, *ChemSusChem*, 2016, **9**(12), 1490–1497, DOI: 10.1002/CSSC.201600165.

20 K. Vighnesh, S. Wang, H. Liu and A. L. Rogach, Hot-Injection Synthesis Protocol for Green-Emitting Cesium Lead Bromide Perovskite Nanocrystals, *ACS Nano*, 2022, **16**(12), 19618–19625, DOI: 10.1021/ACSNANO.2C11689/ASSET/IMAGES/LARGE/NN2C11689_0004.JPEG.

21 X. Liu, Y. Li, H. Ding, L. Chen, S. Du, Z. Chai and Q. Huang, Topotactic Transition of Ti4AlN3 MAX Phase in Lewis Acid Molten Salt, *J. Mater.*, 2023, **9**(6), 1032–1038, DOI: 10.1016/J.JMAT.2023.03.012.

22 W. B. Wang, X. Zhong, Z. Y. He, Z. X. Wang and P. Z. Zhang, Plasma Niobium Surface Alloying of Pure Titanium and Its Oxidation at 900 °C, *Chin. J. Aeronaut.*, 2007, **20**(2), 111–114, DOI: 10.1016/S1000-9361(07)60015-6.

23 H. E. Lai, R. M. S. Yoo, A. Djire and P. B. Balbuena, Investigation of the Vibrational Properties of 2D Titanium Nitride MXene Using DFT, *J. Phys. Chem. C*, 2024, **128**(8), 3327–3342, DOI: 10.1021/ACS.JPCC.3C06717/ASSET/IMAGES/LARGE/JP3C06717_0012.JPEG.

24 A. Balvanz, K. S. Bayikadi, Z. Liu, T. S. Ie, J. A. Peters and M. G. Kanatzidis, Unveiling the Monoclinic Phase in CsPbBr3-XClx Perovskite Crystals, Phase Transition Suppression and High Energy Resolution γ-Ray Detection, *J. Am. Chem. Soc.*, 2024, **146**, 31836–31848, DOI: 10.1021/JACS.4C10872/ASSET/IMAGES/LARGE/JA4C10872_0006.JPEG.

25 J. Casanova-Chafer, R. Garcia-Aboal, K. Mego, S. B. Malik, P. Atienzar and E. Llobet, Lead-Free Perovskite Nanocrystals Decorating Graphene for Detecting Nerve Agents, *ACS Appl. Electron. Mater.*, 2024, **6**(9), 6974–6981, DOI: 10.1021/ACSAELM.4C01220/SUPPL_FILE/EL4C01220_SI_001.PDF.

26 J. Low, L. Zhang, T. Tong, B. Shen and J. Yu, TiO2/MXene Ti3C2 Composite with Excellent Photocatalytic CO2 Reduction Activity, *J. Catal.*, 2018, **361**, 255–266, DOI: 10.1016/J.JCAT.2018.03.009.

27 S. Akhtar, S. Roy, T. T. Tran, J. Singh, A. S. Sharbirin and J. Kim, Low Temperature Step Annealing Synthesis of the Ti2AlN MAX Phase to Fabricate MXene Quantum Dots, *Appl. Sci.*, 2022, **12**(9), 4154, DOI: 10.3390/APP12094154.

28 A. S. Sharbirin, S. Roy, T. T. Tran, S. Akhtar, J. Singh, D. L. Duong and J. Kim, Light-Emitting Ti2N (MXene) Quantum Dots: Synthesis, Characterization and Theoretical Calculations, *J. Mater. Chem. C*, 2022, **10**(16), 6508–6514, DOI: 10.1039/D2TC00568A.

29 P. Mandal, A. Roy, S. Mannar and R. Viswanatha, Growth Mechanistic Insights into Perovskite Nanocrystals: Dimensional Growth, *Nanoscale Adv.*, 2020, **2**(11), 5305–5311, DOI: 10.1039/D0NA00732C.

30 K. Mabhouti, P. Norouzzadeh and M. Taleb-Abbasi, Effects of Fe, Co, or Ni Substitution for Mn on $La_{0.7}Sr_{0.3}MnO_3$ Perovskite: Structural, Morphological, and Optical Analyses, *J. Non-Cryst. Solids*, 2023, **610**, 122283, DOI: 10.1016/J.JNONCRYSOL.2023.122283.

31 M. I. Saleem, S. Yang, M. Sulaman, J. Hu, P. V. Chandrasekar, Y. Shi, R. Zhi, A. Batool and B. Zou, All-Solution-Processed UV-IR Broadband Trilayer Photodetectors with CsPbBr3 Colloidal Nanocrystals as Carriers-Extracting Layer, *Nanotechnology*, 2020, **31**(16), 165502, DOI: 10.1088/1361-6528/AB667B.

32 A. J. Chacón-García, H. G. Baldovi, A. A. Babaryk, A. Rodríguez-Diéguez, S. Navalón, Y. Pérez, H. García and P. Horcajada, Robust Hybrid Bismuth Perovskites as Potential Photocatalysts for Overall Water Splitting, *Nano Res.*, 2024, **17**(5), 4593–4601, DOI: 10.1007/S12274-023-6254-1/METRICS.

33 P. Salcedo-Abraira, R. Serrano-Nieto, C. Biglione, M. Cabrero-Antonino, S. M. F. Vilela, A. A. Babaryk, D. Tilve-Martínez, A. Rodriguez-Diéguez, S. Navalón, H. García and P. Horcajada, Two Cu-Based Phosphonate Metal-Organic Frameworks as Efficient Water-Splitting Photocatalysts, *Chem. Mater.*, 2023, **35**(11), 4211–4219, DOI: 10.1021/ACS.CHEMMATER.3C00054/SUPPL_FILE/CM3C00054_SI_003.CIF.

34 K. Mego, P. Ruiz-Campos, H. G. Baldoví and P. Atienzar, OER Activity Promoted by Organic Ligand-Free Cs2Pt(Cl, Br)6 Perovskite Photocatalyst for Solar-Driven Water Splitting, *Adv. Energy Sustainability Res.*, 2025, 2500105, DOI: 10.1002/AESR.202500105.

35 A. Pan, X. Ma, S. Huang, Y. Wu, M. Jia, Y. Shi, Y. Liu, P. Wangyang, L. He and Y. Liu, CsPbBr3 Perovskite Nanocrystal Grown on MXene Nanosheets for Enhanced Photoelectric Detection and Photocatalytic CO2 Reduction, *J. Phys. Chem. Lett.*, 2019, **10**(21), 6590–6597, DOI: 10.1021/acs.jpclett.9b02605.

36 X. Tang, Z. Zu, Z. Zang, Z. Hu, W. Hu, Z. Yao, W. Chen, S. Li, S. Han and M. Zhou, CsPbBr3/Reduced Graphene Oxide Nanocomposites and Their Enhanced Photoelectric Detection Application, *Sens. Actuators, B*, 2017, **245**, 435–440, DOI: 10.1016/J.SNB.2017.01.168.

37 J. Casanova-Chafer, R. Garcia-Aboal, E. Llobet and P. Atienzar, Enhanced CO2 Sensing by Oxygen Plasma-Treated Perovskite-Graphene Nanocomposites, *ACS Sens.*, 2024, **9**(2), 830–839, DOI: 10.1021/ACSSENSORS.3C02166/ASSET/IMAGES/LARGE/SE3C02166_0008.JPEG.

38 J. A. Peters, Z. Liu, R. Yu, K. M. McCall, Y. He, M. G. Kanatzidis and B. W. Wessels, Carrier Recombination Mechanism in CsPbB R3 Revealed by Time-Resolved Photoluminescence Spectroscopy, *Phys. Rev. B*, 2019, **100**(23), 235305, DOI: 10.1103/PHYSREVB.100.235305/FIGURES/6/MEDIUM.

39 C. Maduwanthi, C. A. Jong, W. S. Mohammed and S. H. Hsu, Stability and Photocurrent Enhancement of Photodetectors by Using Core/Shell Structured CsPbBr3/TiO2 Quantum Dots and 2D Materials, *Nanoscale Adv.*, 2024, **6**(9), 2328–2336, DOI: 10.1039/D3NA01129A.

40 D. Fang, F. He, J. Xie and L. Xue, Calibration of Binding Energy Positions with C1s for XPS Results, *J. Wuhan Univ. Technol., Mater. Sci. Ed.*, 2020, **35**(4), 711–718, DOI: 10.1007/S11595-020-2312-7/METRICS.

41 M. Li, X. Zhang, K. Matras-Postolek, H. S. Chen and P. Yang, An Anion-Driven Sn2+ Exchange Reaction in CsPbBr3 Nanocrystals towards Tunable and High Photoluminescence, *J. Mater. Chem. C*, 2018, **6**(20), 5506–5513, DOI: 10.1039/C8TC00990B.

42 X. Liu, S. Ren, Z. Li, J. Guo, S. Yi, Z. Yang, W. Hao, R. Li and J. Zhao, Flexible Transparent High-Efficiency Photoelectric Perovskite Resistive Switching Memory, *Adv. Funct. Mater.*, 2022, **32**(38), 2202951, DOI: 10.1002/ADFM.202202951.

43 P. Pandey, A. Sengupta, S. Parmar, U. Bansode, S. Gosavi, A. Swarnkar, S. Muduli, A. D. Mohite and S. Ogale, CsPbBr3-Ti3C2T x MXene QD/QD Heterojunction: Photoluminescence Quenching, Charge Transfer, and Cd Ion Sensing Application, *ACS Appl. Nano Mater.*, 2020, **3**(4), 3305–3314, DOI: 10.1021/ACSANM.0C00051/SUPPL_FILE/AN0C00051_SI_001.PDF.

44 X. Di, L. Shen, J. Jiang, M. He, Y. Cheng, L. Zhou, X. Liang and W. Xiang, Efficient White LEDs with Bright Green-Emitting CsPbBr3 Perovskite Nanocrystal in Mesoporous Silica Nanoparticles, *J. Alloys Compd.*, 2017, **729**, 526–532, DOI: 10.1016/J.JALLCOM.2017.09.213.

45 J. Halim, M. R. Lukatskaya, K. M. Cook, J. Lu, C. R. Smith, L. Å. Näslund, S. J. May, L. Hultman, Y. Gogotsi, P. Eklund and M. W. Barsoum, Transparent Conductive Two-Dimensional Titanium Carbide Epitaxial Thin Films, *Chem. Mater.*, 2014, **26**(7), 2374–2381, DOI: 10.1021/CM500641A/SUPPL_FILE/CM500641A_SI_001.PDF.

46 J. Halim, K. M. Cook, M. Naguib, P. Eklund, Y. Gogotsi, J. Rosen and M. W. Barsoum, X-Ray Photoelectron Spectroscopy of Select Multi-Layered Transition Metal Carbides (MXenes, *Appl. Surf. Sci.*, 2016, **362**, 406–417, DOI: 10.1016/J.APSUSC.2015.11.089.

47 C. Cheng, B. He, J. Fan, B. Cheng, S. Cao and J. Yu, An Inorganic/Organic S-Scheme Heterojunction H2-Production Photocatalyst and Its Charge Transfer Mechanism, *Adv. Mater.*, 2021, **33**(22), 2100317, DOI: 10.1002/ADMA.202100317.

48 Q. Tang, Z. Sun, S. Deng, H. Wang and Z. Wu, Decorating G-C3N4 with Alkalinized Ti3C2 MXene for Promoted Photocatalytic CO2 Reduction Performance, *J. Colloid Interface Sci.*, 2020, **564**, 406–417, DOI: 10.1016/J.JCIS.2019.12.091.

49 L. Liuhe, X. Lifang and M. Xinxin, XPS of Ti + TiN + (N,C) Multilayer Films Deposited by Filtered Cathodic Arc Deposition with Controlled Feed Gas Flow Rate, *Surf. Coat. Technol.*, 1999, **120–121**, 618–621, DOI: 10.1016/S0257-8972(99)00426-0.

50 D. C. Coyac, E. Kabachkov, E. Kurkin, N. Vershinin, I. Balikhin, V. Berestenko, A. Michtchenko, Y. Shulga, D. C. Coyac, E. Kabachkov, E. Kurkin, N. Vershinin, I. Balikhin, V. Berestenko, A. Michtchenko and Y. Shulga, Pt Supported on Plasma-Chemical Titanium Nitride for Efficient Room-Temperature CO Oxidation, *Mod. Res. Catal.*, 2022, **11**(1), 1–11, DOI: 10.4236/MRC.2022.111001.

51 H. Zhu, Z. Qin, W. Shan, W. Shen and J. Wang, Pd/CeO2–TiO2 Catalyst for CO Oxidation at Low Temperature: A TPR Study with H2 and CO as Reducing Agents, *J. Catal.*, 2004, **225**(2), 267–277, DOI: 10.1016/J.JCAT.2004.04.006.

52 C. Guo, L. Wang, Y. Tang, Z. Yang, Y. Zhao, Y. Jiang, X. Wen and F. Wang, Enhanced Photo-Thermal CO2 Methanation with Tunable RuxNi1-x Catalytic Sites: Alloying Beyond Pure Ru, *Adv. Funct. Mater.*, 2025, **35**(6), 2414931, DOI: 10.1002/adfm.202414931.

53 J. Wang, K. Vikrant, S. A. Younis, K. H. Kim and P. M. Heynderickx, Low-Temperature Oxidative Removal of Benzene from the Air Using Titanium Carbide (MXene)-Supported Platinum Catalysts, *Chemosphere*, 2024, **350**, 141114, DOI: 10.1016/J.CHEMOSPHERE.2024.141114.

54 G. I. Panov, K. A. Dubkov and E. V. Starokon, Active Oxygen in Selective Oxidation Catalysis, *Catal. Today*, 2006, **117**(1–3), 148–155, DOI: 10.1016/J.CATTOD.2006.05.019.

55 N. G. Akalework, C. J. Pan, W. N. Su, J. Rick, M. C. Tsai, J. F. Lee, J. M. Lin, L. D. Tsai and B. J. Hwang, Ultrathin TiO2-Coated MWCNTs with Excellent Conductivity and SMSI Nature as Pt Catalyst Support for Oxygen Reduction Reaction in PEMFCs, *J. Mater. Chem.*, 2012, **22**(39), 20977–20985, DOI: 10.1039/C2JM34361D.

56 Y. Tang, H. Wang, C. Guo, Z. Yang, T. Zhao, J. Liu, Y. Jiang, W. Wang, Q. Zhang, D. Wu, Y. Zhao, X. D. Wen and F. Wang, Ruthenium–Cobalt Solid-Solution Alloy Nanoparticles for Enhanced Photopromoted Thermocatalytic CO2 Hydrogenation to Methane, *ACS Nano*, 2024, **18**(17), 11449–11461, DOI: 10.1021/ACSNANO.4C02416.

57 W. N. R. Wan Isahak, Z. A. Che Ramli, M. W. Mohamed Hisham and M. A. Yarmo, The Formation of a Series of Carbonates from Carbon Dioxide: Capturing and Utilisation, *Renewable Sustainable Energy Rev.*, 2015, **47**, 93–106, DOI: 10.1016/J.RSER.2015.03.020.

58 S. Grimme, J. Antony, S. Ehrlich and H. Krieg, A Consistent and Accurate Ab Initio Parametrization of Density Functional Dispersion Correction (DFT-D) for the 94 Elements H-Pu, *J. Chem. Phys.*, 2010, **132**(15), 154104, DOI: 10.1063/1.3382344/926936.

59 S. Grimme, S. Ehrlich and L. Goerigk, Effect of the Damping Function in Dispersion Corrected Density Functional Theory, *J. Comput. Chem.*, 2011, **32**(7), 1456–1465, DOI: 10.1002/JCC.21759;JOURNAL:JOURNAL:1096987X;WGROUP:STRING:PUBLICATION.

60 A. Jurado, K. Ibarra, Á. Morales-García, F. Viñes and F. Illas, Adsorption and Activation of CO2 on Nitride MXenes: Composition, Temperature, and Pressure Effects, *Chem. Phys. Chem.*, 2021, **22**(23), 2456–2463, DOI: 10.1002/CPHC.202100600;REQUESTEDJOURNAL:JOURNAL:14397641;PAGEGROUP:STRING:PUBLICATION.

61 R. Morales-Salvador, J. D. Gouveia, Á. Morales-García, F. Viñes, J. R. B. Gomes and F. Illas, Carbon Capture and Usage by MXenes, *ACS Catal.*, 2021, **11**(17), 11248–11255, DOI: 10.1021/ACSCATAL.1C02663.

62 D. C. Sorescu, J. Lee, W. A. Al-Saidi and K. D. Jordan, CO_2 Adsorption on TiO_2(110) Rutile: Insight from Dispersion-Corrected Density Functional Theory Calculations and Scanning Tunneling Microscopy Experiments, *J. Chem. Phys.*, 2011, **134**(10), 104707, DOI: 10.1063/1.3561300/70606.

63 W. J. Yin, M. Krack, B. Wen, S. Y. Ma and L. M. Liu, CO_2 Capture and Conversion on Rutile TiO_2(110) in the Water Environment: Insight by First-Principles Calculations, *J. Phys. Chem. Lett.*, 2015, **6**(13), 2538–2545, DOI: 10.1021/ACS.JPCLETT.5B00798.

64 D. C. Sorescu, J. Lee, W. A. Al-Saidi and K. D. Jordan, Coadsorption Properties of CO_2 and H_2O on TiO_2 Rutile (110): A Dispersion-Corrected DFT Study, *J. Chem. Phys.*, 2012, **137**(7), 74704, DOI: 10.1063/1.4739088/192030.

65 G. B. Raupp and J. A. Dumesic, Adsorption of Carbon Monoxide, Carbon Dioxide, Hydrogen, and Water on Titania Surfaces with Different Oxidation States, *J. Phys. Chem.*, 2002, **89**(24), 5240–5246, DOI: 10.1021/J100270A024.

66 B. Wei and M. Calatayud, Hydrogen Activation on Anatase TiO2: Effect of Surface Termination, *Catal. Today*, 2022, **397–399**, 113–120, DOI: 10.1016/J.CATTOD.2021.11.020.

67 M. López, Á. Morales-García, F. Viñes and F. Illas, Thermodynamics and Kinetics of Molecular Hydrogen Adsorption and Dissociation on MXenes: Relevance to Heterogeneously Catalyzed Hydrogenation Reactions, *ACS Catal.*, 2021, **11**(21), 12850–12857, DOI: 10.1021/ACSCATAL.1C03150.

68 J. Fu, K. Jiang, X. Qiu, J. Yu and M. Liu, Product Selectivity of Photocatalytic CO2 Reduction Reactions, *Mater. Today*, 2020, **32**, 222–243, DOI: 10.1016/J.MATTOD.2019.06.009.

69 Y. Zhang, W. Chen, M. Zhou, G. Miao and Y. Liu, Efficient Photocatalytic CO2Reduction by the Construction of Ti3C2/CsPbBr3QD Composites, *ACS Appl. Energy Mater.*, 2021, **4**(9), 9154–9165, DOI: 10.1021/ACSAEM.1C01406/ASSET/IMAGES/MEDIUM/AE1C01406_M008.GIF.

70 E. Palomares, J. N. Clifford, S. A. Haque, T. Lutz and J. R. Durrant, Control of Charge Recombination Dynamics in Dye Sensitized Solar Cells by the Use of Conformally Deposited Metal Oxide Blocking Layers, *J. Am. Chem. Soc.*, 2003, **125**(2), 475–482, DOI: 10.1021/JA027945W/ASSET/IMAGES/LARGE/JA027945WF00006.JPEG.

71 P. Atienzar, T. Ishwara, B. N. Illy, M. P. Ryan, B. C. O'Regan, J. R. Durrant and J. Nelson, Control of Photocurrent Generation in Polymer/ZnO Nanorod Solar Cells by Using a Solution-Processed TiO_2 Overlayer, *J. Phys. Chem. Lett.*, 2010, **1**(4), 708–713, DOI: 10.1021/JZ900356U/ASSET/IMAGES/LARGE/JZ-2009-00356U_0003.JPEG.

72 X. Chang, T. Wang and J. Gong, CO_2 Photo-Reduction: Insights into CO_2 Activation and Reaction on Surfaces of Photocatalysts, *Energy Environ. Sci.*, 2016, **9**(7), 2177–2196, DOI: 10.1039/C6EE00383D.

73 L. Hu, X. Sai, X. Liu, Z. Chen, G. Wang and X. Yi, Influence of Environmental Conditions on Electrocatalytic CO_2 Reduction, *ChemCatChem*, 2024, **16**(6), e202301335, DOI: 10.1002/CCTC.202301335.